Micromotion-enhanced fast entangling gates for trapped-ion quantum computing

Alexander K. Ratcliffe [ORCID],[*] Lachlan M. Oberg, and Joseph J. Hope
Department of Quantum Science, RSPE, Australian National University, Canberra, ACT 0200, Australia

Radio-frequency-induced micromotion in trapped ion systems is typically minimized or circumvented to avoid off-resonant couplings for adiabatic processes such as multi-ion gate operations. Nonadiabatic entangling gates (so-called "fast gates") do not require resolution of specific motional sidebands and are, therefore, not limited to time scales longer than the trapping period. We find that fast gates designed for micromotion-free environments have a significantly reduced fidelity in the presence of micromotion. We show that when fast gates are designed to account for the radio-frequency-induced micromotion, they can, in fact, outperform fast gates in the absence of micromotion. The state-dependent force due to the laser induces energy shifts that are amplified by the state-independent forces producing the micromotion. This enhancement is present for all trapping parameters and is robust to realistic sources of experimental error. This result paves the way for fast two-qubit entangling gates on scalable two-dimensional architectures, where micromotion is necessarily present on at least one interior axis.

I. INTRODUCTION

Quantum computing offers the promise of boosting our current computational capabilities, outperforming certain known classical algorithms, and allowing tractable simulations of complex quantum systems [1]. To realize this potential, a quantum information processing (QIP) architecture must be able to scale to large numbers of qubits. Many platforms have been proposed as QIP architectures including superconducting qubits [2], defect centers in diamonds [3], single photons [4], NMR [5], topological qubits [6], quantum dots [7], and spin-spin interactions in silicon donor sites [8]. Significant progress towards the requirements for scalable quantum computing has been made on these platforms, demonstrating single- and two-qubit fidelities [9–14] above a 98% fault-tolerant threshold. However, these platforms have been limited either by scalability or by the number of high-fidelity operations achievable before state decoherence. To date, trapped ions have been a front-runner of QIP architectures, making a number of important demonstrations towards scalable fault-tolerant quantum computing. These have included the deterministic entanglement between 20 atomic qubits [15], the use of hybrid quantum-classical computer to find the ground-state energy of simple molecules [16], the topological protection and error correction of a qubit state [17], and analog quantum simulation of phase transitions using 53 qubits [18]. These are important demonstrations of the control and procedures required for scalable fault-tolerant quantum computing.

A key limitation in all QIP platforms is the number of independent, high-fidelity two-qubit gate operations that can be achieved within the decoherence time of the qubit. Fault-tolerant quantum computation requires that enough of these operations can be conducted with high enough fidelities to correct for errors in both the gate operations and state decoherence. For surface codes, these limits are modest and can enable fault-tolerant computation with fidelities as low as 98% [9]. In this paper we use a more stringent threshold of 99.98% as a guide, achievable using a Bacon-Shor code with $n = 10$ [19]. Numerous implementations of sideband-resolving adiabatic gates have demonstrated fidelities above the 98% fault-tolerant threshold. For example, Bell-state fidelities of 99.9% and above [20,21] have been demonstrated, and a gate fidelity of 99.8% has been demonstrated with randomized benchmarking [22]. With the larger numbers of qubits needed for computation beyond classical capability these gates require longer operation times [23], preventing classically unrealizable computation within the decoherence time.

Fast gates using ultrafast pulses are poised to resolve this situation [24–27]. These gate schemes use state-dependent kicks (SDKs) from ultrafast π pulses to the ions, inducing state-dependent motion. This results in a state-dependent phase shift mediated by the Coulomb interaction. High-fidelity gates 100–1000 times faster than sideband-resolving gates can theoretically be achieved with current laser technology [26,28]. Schemes with ultrafast pulses have recently been used to create Schrödinger cat states [29] and to prepare Bell states [30]. Similar schemes using an amplitude-modulated continuous laser creating a dipole force to prepare Bell states have also been demonstrated [31]. So far, these schemes have only been applied to linear Paul traps in which the ions are arranged linearly in a common trap. This architecture poses some difficulties in scaling to larger numbers of qubits. When the number of ions in the trap is increased, the longitudinal trapping frequency must be lowered to prevent buckling of the ion chain, which then slows both adiabatic and fast gates conducted on the longitudinal motional modes [26,32].

Ion traps use an oscillating radio-freqency (RF) potential to generate a three-dimensional (3D) trapping potential. The resulting dynamics approximate a simple harmonic oscillator,

_____
[*]alexander.ratcliffe@anu.edu.au

but with the addition of a rapid oscillation. This fast oscillation induced by the oscillating RF potential is referred to as micromotion [33] or intrinsic micromotion. While for a perfect trap it is entirely deterministic and entirely in the radial plane, trap imperfections cause this motion to be complicated and coupled into the axial modes. This is typically called "excess micromotion," and considerable effort goes into reducing this in experiments. Even in perfect traps, the "intrinsic" micromotion still exists. It has largely been treated as an undesirable effect, as it complicates the use of the radial mode, which would otherwise provide the benefit of operating at a higher trapping frequency. This effect is minimized for adiabatic entangling gates, where it has been shown that it does not inhibit the ability to apply high-fidelity entangling operations for sideband-resolving geometric phase gates using a continuously shaped laser pulse [34] or by addressing the micromotion sidebands [21,35].

We show that fast gates are more affected by micromotion and that gates designed without awareness of the micromotion have dramatically reduced fidelity. We speculate that micromotion may have been a contributing factor to the low fidelities observed in [30]. Micromotion would also impact the operation of gates in 2D architectures such as microtraps [36], as the coupled modes in the gate scheme cannot all be orthogonal to the micromotion axes.

Fortunately, designing fast gates with foreknowledge of the micromotion leads to good news: we find that the fidelity can be *increased* for some experimentally accessible parameter regimes. It is interesting that the state-independent forces in micromotion can in fact enhance the rate of phase accumulation from the state-dependent forces of the laser pulses. This improvement is present both in the radial modes of a linear Paul trap and in the transverse modes of a microtrap system and exists for all trap parameters. We also show that these gates are robust to realistic sources of experimental error.

II. MODEL

Ions can be trapped in three dimensions by a time-averaged potential. The time-dependent potential used to generate this trapping is given by

$$\Phi(x, y, z, t) = \frac{U}{2}(\alpha x^2 + \beta y^2 + \gamma z^2) + \cos(\omega_{\text{RF}}t + \phi_{\text{RF}})$$
$$\times \frac{\tilde{U}}{2}(\alpha' x^2 + \beta' y^2 + \gamma' z^2), \quad (1)$$

which has previously been shown to lead to motion of the form [33]

$$x(t) = A e^{i\frac{\beta\omega_{\text{RF}}}{2}t} \sum_{j=-\infty}^{\infty} C_j e^{ij(\omega_{\text{RF}}t + \phi_{\text{RF}})}$$
$$+ B e^{-i\frac{\beta\omega_{\text{RF}}}{2}t} \sum_{j=-\infty}^{\infty} C_j e^{-ij(\omega_{\text{RF}}t + \phi_{\text{RF}})}, \quad (2)$$

where A and B are arbitrary constants determined by boundary conditions, β_x, a_x, and q_x are given by

$$\beta_x \approx \sqrt{a_x + \frac{q_x^2}{2}}, \quad a_x = \frac{4Z|e|U\alpha}{m\omega_{\text{RF}}^2}, \quad q_x = -\frac{2Z|e|\tilde{U}\alpha'}{m\omega_{\text{RF}}^2},$$
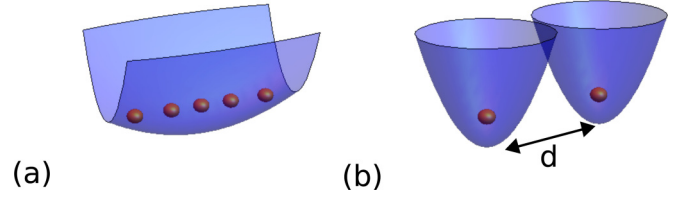

FIG. 1. (a) Diagram of a linear ion chain, as would be found in linear Paul trap experiments. The lasers used to conduct the two-qubit gates considered in this paper are applied orthogonal to the axis along which the ions are aligned. (b) Diagram of the ions trapped in individual microtraps. In this case, the gates considered are conducted using lasers parallel to the ion chain.

and the coefficients $\{C_j\}$ are determined by a continued fraction with respect to β_x, a_x, and q_x [33]. This equation describes a motion with a secular trapping frequency of $\omega = (1/2)\beta_x\omega_{\text{RF}}$ and an additional high-frequency oscillation, which is referred to as micromotion. To ensure sufficient numerical convergence of the optimized gates in this work, it is necessary to take the above expansion over at least $j = -3$ to $j = 3$ for values of q greater than ~ 0.3. In the work presented here the value β_x is found using the MathieuCharacteristicExponent function provided by Mathematica. This gives an accurate value for the exponent for all values of a and q.

In this work we consider fast gates conducted between neighboring ions in a linear chain of microtraps using the motional modes aligned parallel to the chain of ions and gates between neighboring ions in a linear Paul trap using their radial modes. This is shown in Figs. 1(a) and 1(b), respectively, and the potentials describing these architectures are given by V_M and V_P, respectively,

$$V_M = \frac{e^2}{4\pi\varepsilon_0} \sum_{i=1}^{N-1} \sum_{j=i+1}^{N} \frac{1}{((j-i)d + x_j - x_i)}$$
$$+ \frac{1}{2}M\frac{a - 2q\cos(\omega_{\text{RF}}t)}{4}\omega_{\text{RF}}^2 \sum_{i=1}^{N} x_i^2, \quad (3)$$

$$V_P = \frac{e^2}{4\pi\varepsilon_0} \sum_{i=1}^{N-1} \sum_{j=i+1}^{N} \frac{1}{\sqrt{(x_j - x_i)^2 + (z_j - z_i)^2}}$$
$$+ \frac{1}{2}\frac{M}{4}\omega_{\text{RF}}^2 \sum_{i=1}^{N} \left(a_z z_i^2 + (a_x - 2q_x\cos(\omega_{\text{RF}}t))x_i^2\right), \quad (4)$$

where x_i is the deviation of the ith ion in the chain from its equilibrium, d is the separation between each microtrap, ω_{RF} is the RF drive frequency used to generate the trapping potential, M is the ion mass, and N the number of ions in the chain. We consider gates between neighboring ions using the modes that are only coupled to the x axis for the microtrap array model and the z axis in the linear Paul trap model. We drop the subscripts for a, q, and β in the remaining discussion.

We use a normal mode expansion to describe the classical coupled motion of the ions. This approximates the motion in terms of N oscillatory modes, each mode described by some frequency of oscillation ω_p and coupling to the ions $\vec{b}_p$. This

is done by linearizing the potential around the ions' stationary points and is valid for sufficiently small displacements of the ions around their stationary points. We use the secular trapping period of the common motional mode $2\pi/\omega_{\mathrm{COM}}$ as the natural time scale, as it simplifies the gate analysis, where ω_{COM} can be expressed as $\omega_{\mathrm{COM}} = \frac{1}{2}\beta\omega_{\mathrm{RF}}$. We then use the nondimensional time τ given by $\tau = \frac{\beta\omega_{\mathrm{RF}}}{4\pi}t$. This will then give the motion as

$$x_i = A_p b_p^i e^{i2\pi\frac{\omega_p}{\omega}\tau} \sum_{j=-\infty}^{\infty} C_j e^{\frac{i4\pi j(\tau+\phi_{\mathrm{RF}})}{\beta}}$$
$$+ B_p b_p^i e^{-i2\pi\frac{\omega_p}{\omega}\tau} \sum_{j=-\infty}^{\infty} C_j e^{-\frac{i4\pi j(\tau+\phi_{\mathrm{RF}})}{\beta}}, \qquad (5)$$

with the amplitudes of each mode A_p and B_p and the phase of the RF drive ϕ_{RF} relative to the time $\tau = 0$, determined by the choice of initial conditions. We note that to match the phase evolution of the ordinary differential equation, the first-order solution is not sufficient, and we need to take the Fourier expansion in Eq. (5) to the third term. While the frequency of the common motional mode will remain the same as the secular frequency of the single-ion system ω, the motion of the other secular modes will be different from that of those derived in the absence of micromotion. To determine the motion of the secular modes, it is necessary to solve the Hill equations resulting from the eigendecomposition of the coupled ordinary different equations linearized about the equilibrium position. The Hill equations for each of the modes will take the form

$$-\frac{(2\pi)^2}{\beta^2} \sum_{j=0}^{\infty} h_{j,p} \cos\left(\frac{4\pi\tau}{\beta}\right)\Upsilon_p = \frac{d^2\Upsilon_p}{d\tau^2}, \qquad (6)$$

where Υ_p is some coordinate describing the modes' displacement, and the coefficients $h_{j,p}$ can be found in terms of the equilibrium position,

$$h_{j,p} = \int_0^{\beta/2} \frac{4\beta\lambda \cos\left(\frac{4\pi j\tau}{\beta}\right)}{(\delta + 2x_{0,1}(\tau))^3} d\tau. \qquad (7)$$

We truncate Eq. (6) to the first-order Fourier term, which is of the form of a Mathieu equation,

$$-\frac{(2\pi)^2}{\beta^2}\left(a_p - 2q_p \cos\left(\frac{4\pi\tau}{\beta}\right)\right)\Upsilon_p = \frac{d^2\Upsilon_p}{d\tau^2}, \qquad (8)$$

where a_p and q_p are now mode specific. These can then be used to find β_p, which can be used to find the secular mode frequency ω_p as

$$\omega_p = \beta_p \omega_{\mathrm{RF}}. \qquad (9)$$

In the case of a linear Paul trap the equilibrium remains constant in time and the linearization results in a change in the parameter a_p for that mode. This will be given by

$$a_p = a - \frac{\beta^2\kappa^2}{(2\pi)^2}. \qquad (10)$$

For a microtrap array it is necessary to find the periodic crystal solution. This is the motion that the ions will undertake without any excitation of the secular modes and may

be regarded as a form of "excess" micromotion in previous analyses. This motion will be periodic with the RF-drive frequency and will take the form

$$x_{0,i}(\tau) = u_{0,i} + \sum_{j=1}^{\infty} u_{j,i} \cos\left(\frac{4\pi j\tau}{\beta}\right) + \sum_{j=1}^{\infty} w_{j,i} \sin\left(\frac{4\pi j\tau}{\beta}\right). \qquad (11)$$

In particular, the two-ion case will take the form

$$x_{0,1}(\tau) = u_0 + \sum_{j=1}^{\infty} u_j \cos\left(\frac{4\pi j\tau}{\beta}\right),$$
$$x_{0,2}(\tau) = -u_0 - \sum_{j=1}^{\infty} u_j \cos\left(\frac{4\pi j\tau}{\beta}\right). \qquad (12)$$

The coefficients can be found using a continued series of matrix determinants [37]. In this paper, we use an iterative method, whereby an initial guess of this motion is made and improved over a number of iterations. This is achieved by using the trial solution as the initial condition for a numerical ODE simulation of the motion for a time close to an integer number of secular trap periods. The average position is then used to adjust the constant component of the periodic crystal solution. The Fourier components then form the coefficients a_n. We have found that this method converges to the correct periodic crystal solution.

III. GATE SCHEME AND OPTIMIZATION

A description of many of the features of this scheme and optimization has been presented in [28] and is presented here for convenience to the reader. Fast gates using ultrafast pulses are implemented by illuminating a pair of ions with a series of counter-propagating π pulse pairs. Each of these counter-propagating pulse pairs induces a state-dependent momentum kick on the incident ions, appearing as vertical jumps in a phase-space diagram. By appropriately choosing the arrival times and arrival orderings of the pulse pairs it is possible to implement an entangling gate. The fully entangling gate operation that can be implemented using this method is the controlled phase (CPhase) gate, also referred to as a controlled-zz gate, given as

$$\hat{U}_{\mathrm{CPhase}} = e^{i\frac{\pi}{4}\sigma_1^z\sigma_2^z}. \qquad (13)$$

To enable a more tractable optimization of the gate fidelity, the pulse pairs are organized into groups of pulses. These groups are assumed to provide an instantaneous momentum kick consisting of $\vec{z}$ pulse pairs at times $\vec{t}$. We use a gate scheme that is a generalization of the fast robust antisymmetric gate (FRAG) scheme [27] (Fig. 2), which is in turn a variant of the GZC scheme [38]. It consists of six groups of counter-propagating π pulses incident on the ions to be entangled. The timings of theses pulses and the number of pulses in each pulse group are given by the vectors $\underline{t}$ and $\underline{z}$, respectively:

$$\underline{t} = (-\tau_1, -\tau_2, -\tau_3, \tau_3, \tau_2, \tau_1),$$
$$\underline{z} = (-n, 2n, -2n, 2n, -2n, n). \qquad (14)$$

The sign of the components of $\underline{z}$ corresponds to changing the direction of the initially incident pulse, and the factor of n is an integer that characterizes the overall scale of numbers of pulses in each pulse group.

To produce a high-fidelity CPhase gate the timings (τ_1, τ_2, τ_3) are optimized to give the desired gate. In the original FRAG scheme proposal there was a strict ordering of the magnitude of (τ_1, τ_2, τ_3). In this implementation we do not impose a strict ordering of the times (τ_1, τ_2, τ_3), effectively resulting in a set of six possible pulse schemes. The total gate time τ_G is therefore twice the maximum of the values of τ_1, τ_2, and τ_3.

The optimization was carried out by using a large number of local optimizations within a bounded gate time. The bounds are then incrementally increased and the new region is searched. Using this method, we establish a relationship between the allowed gate time and the gate infidelity.

We use the state-averaged fidelity F as the measure of a gate's performance in this work because it can be calculated with a high efficiency [27,28,39]. Inclusion of the micromotion adds additional terms to the analytic fidelity expression, as detailed in Appendix C. As we are interested in gates with fidelities close to unity, it is sensible to report this in terms of the infidelity $1 - F$. We then simplify this expression for small errors in phase and motional restoration, giving the infidelity expression as

$$1 - F \approx \frac{2}{3}\Delta\phi^2 + \frac{4}{3}\sum_p \left(\frac{1}{2} + \bar{n}_p\right)$$
$$\times \left((b_p^1)^2 + (b_p^2)^2\right)\Delta P_p^2, \qquad (15)$$

where $\Delta\phi$ is the error in the phase, ΔP_p is the displacement of the pth mode in phase space, b_p^n is the coupling of the pth mode to the jth ion, and $\bar{n}_p$ is the mean phonon occupation of the pth mode. Expressions for $\Delta\phi$ and ΔP_p are given in Eq. (17). We assume a thermal product state, with a mean mode occupation of $\bar{n}_p = 0.1$ throughout this work. This assumption has been the basis throughout previous works [27,28] and has been experimentally demonstrated [40]. For larger mode occupations the infidelity will increase linearly with $\bar{n}_p$. The final quoted infidelities were confirmed by directly integrating the ODEs for the classical phase-space trajectories over the qubit basis states. The enclosed signed area of these trajectories is used to calculate the geometric phase, also known as the Berry phase.

For the purposes of designing fast gates for two-ion systems, traps are well characterized by the dimensionless parameter χ, which is the scaled difference between the breathing and the common motional modes $\chi = \frac{\omega_{BR} - \omega}{\omega}$ in the direction of the laser-induced motion [28]. Expressions for χ in terms of trap parameters depend on the geometry and are given in Appendix B. In a linear Paul trap χ is negative for motion in the radial modes, indicating a phase acquisition rate of the opposite sign to gates conducted using the axial modes. In this case, we optimize for a controlled phase gate with opposite relative phase, which is equivalent up to single-qubit π rotations.

The phase-space trajectories are more complicated for the system evolving with micromotion. This comparison is shown
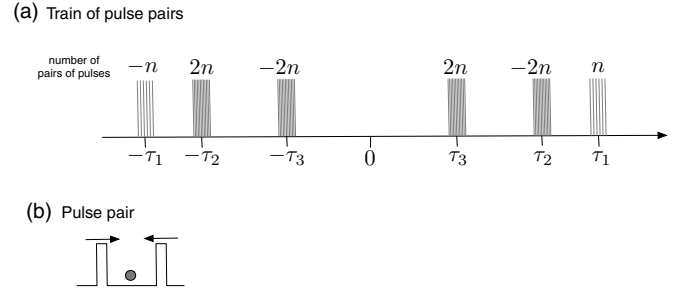

(a) Train of pulse pairs

(b) Pulse pair

FIG. 2. (a) Diagram of the pulse timing for the FRAG scheme. The components z_j of the z vector indicate the number of pairs of pulses that hit the ion at each time τ_j. The sign of z_j indicates which pulse within each pair [shown in (b)] reaches the ion first. This gives the sign of the momentum kick imprinted on the ion.

in Fig. 3. These trajectories can be averaged to remove the rapid oscillation induced by micromotion. In the case where a continuous phase-space displacement is applied to the system, the averaged trajectory will be well approximated by the trajectory of the approximate harmonic trap, provided the interaction is slow with respect to the RF drive. However, when these interactions occur on time scales faster than the RF drive, the averaged phase-space trajectories can differ substantially from those that would be found using a simple harmonic trapping approximation. The SDKs used in this work provide a near-instantaneous momentum kick, considerably faster than the RF oscillation. The averaged phase-space displacements for these kicks will be larger or smaller depending on when they are timed in the RF cycle. We define μ as the relative increase in the maximum displacement of the ions D over the maximum displacement of the ions in a simple harmonic potential D', achieved through a momentum kick. This will be given as

$$\mu \approx \left(1 - \frac{2(\beta^2 + 4)q\cos(\phi_{RF})}{(\beta^2 - 4)^2}\right)^2. \qquad (16)$$

By timing the arrival of the SDKs to particular times in the RF cycle, it is possible to achieve faster gate times using the same number of counter-propagating pulse pairs. Here we investigate a scheme in which the gate is optimized assuming all pulses arrive at the same point in the RF cycle. This assumption simplifies the infidelity expression with the inclusion of micromotion:

$$\Delta P_p = 2\mu\sqrt{\frac{\omega}{\omega_p}}\sum_k z_k \sin(\omega_p t_k),$$

$$\Delta\phi = \left|\sum_p 8\eta^2\mu\frac{\omega}{\omega_p}b_p^1 b_p^2 \sum_{i\neq j} z_i z_j \sin(\omega_p|t_i - t_j|)\right| - \frac{\pi}{4}.$$
$$(17)$$

The factor μ in the acquired phase corresponds to the change in the extent of the phase-space displacements due to locking the π pulses to a particular point in the RF cycle. The presence of this factor in the motional restoration terms would decrease the fidelity of gates optimized without this factor. When it is included in the optimization, the ideal

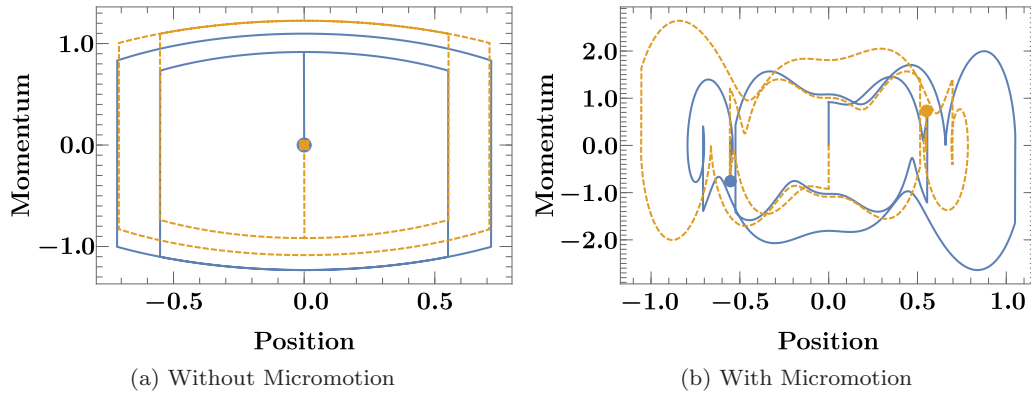(a) Without Micromotion

(b) With Micromotion

FIG. 3. Dimensionless phase-space trajectories of the common motional (solid blue lines) and rocking (dashed orange lines) modes of a two-ion fast gate conducted using the radial modes of a linear Paul trap. (a) Trajectories without micromotion, showing a clear motional restoration indicated by the circular markers at the origin of the plot. The theoretical infidelity of this gate is roughly 10^{-12}. (b) The same fast-gate operation with the inclusion of micromotion. This clearly shows that there is no longer restoration of the modes, indicated by the two markers showing the end of the trajectory far from the origin. The parameters a and q were set to 0.0 and 0.2, respectively; the theoretical infidelity of this gate is now $\sim$0.5.

achievable fidelities are similar to the system in the absence of micromotion. It does, however, increase the sensitivity of the scheme to systematic pulse timing errors. This is an inherent feature of achieving faster gate times, which necessitate larger displacements in phase space.

The values of the parameter μ are shown in Fig. 4 for values of a and q, with the perimeter of the plot marking out the stable trapping regions of the ideal trap. It is noteworthy that not all combinations of a and q presented in Fig. 4 are stable in practice. This is due to the presence of resonances induced by the nonlinearity of the trapping potential or trap imperfections [41–43]. This typically limits experiments to parameter choices with a value of μ less than 2.5. The full expression of μ and its derivation are given in Appendix C.
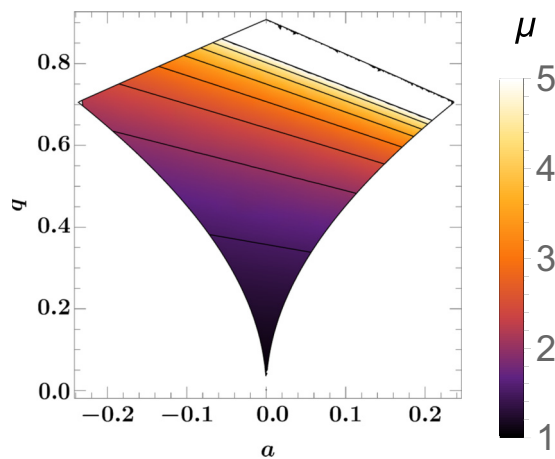

FIG. 4. The values of μ are shown as color gradients over the stable region of trapping parameters a and q. The region to the top right of the image diverges towards ∞, but this is generally not a useful region, as it results from RF frequencies close to the trapping frequencies.

IV. IMPACT OF MICROMOTION AND MICROMOTION ENHANCEMENT

We now look at the effect micromotion has on a two-qubit gate that was optimized for a system without micromotion. We observe a decreasing fidelity as the dynamic trapping potential $\tilde{U}$ is increased, shown in Fig. 5. The dips in these plots corresponds to phases that minimize the effects of micromotion on motional restoration, producing closed phase-space trajectories. Taking into account the effects of a finite repetition rate would further reduce the fidelities shown in Fig. 5. As shown later, micromotion makes fast gate schemes particularly sensitive to the finite repetition rate of the SDKs. The successful implementation of a fast gate using state-dependent kicks therefore requires both accounting for RF-induced micromotion in the optimization process and either using a finite repetition rate sufficiently faster than the RF frequency or taking the finite repetition rate directly into account in the optimization process. The latter is typically computationally prohibitive.

We now examine gates that are designed to operate in the presence of micromotion. The rate of phase acquisition will be maximiezd when the pulses occur at the point in the RF cycle where μ is maximized, corresponding to the time at which the oscillating part of the potential is maximally trapping. We thus examine the case where the repetition rate is locked to the RF drive with a phase between them of $\phi_{RF} = \pi$. The phase ϕ_{RF} is defined in Eq. (1) as the phase of the driving potential at $t = 0$, and this assumption means that it will be the phase of the driving potential for all of our pulses.

We find that the performance of two-qubit gates improves with the amount of micromotion, indicated by the infidelity decreasing with increasing μ, which corresponds to an increasing a and q. This improvement is shown in Fig. 6 for both a microtrap array and the radial modes of a linear Paul trap. Although only one choice of gate parameter n is shown, the improvement is present for all choices of n. The plateaus in the infidelity observed for some gate times can be attributed to the antisymmetric nature of the gate scheme, which is not
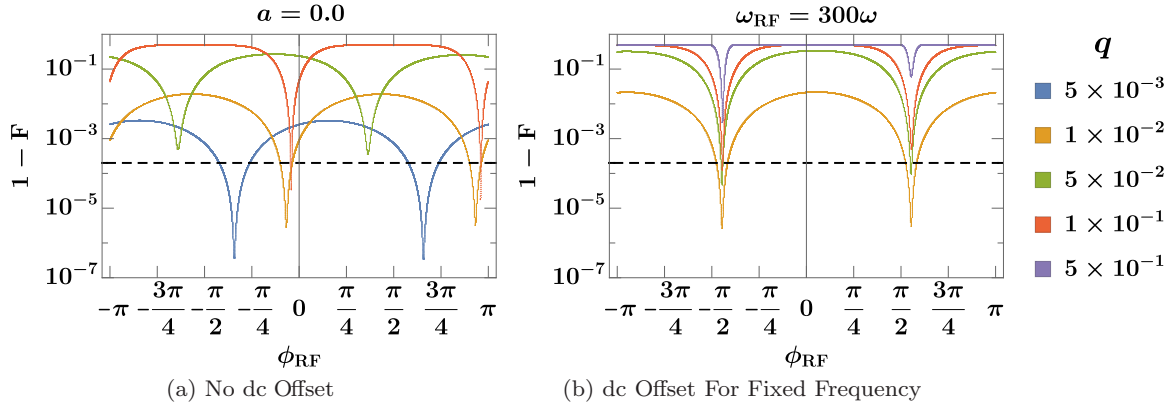
FIG. 5. Gates that are optimized assuming an absence of micromotion typically have a decreasing fidelity under realistic amounts of micromotion. We show infidelities for such gates plotted with respect to the phase offset between the first pulse in the gate and the RF drive. Infidelities are shown for various values of q; the trends in both plots move up (increasing infidelity) with increasing values of q. (a) The value of a is fixed at 0.0 and the values of q are from 5×10^{-3} (lowest-infidelity trend) to 1×10^{-1} (highest-infidelity trend). (b) a is chosen to maintain an RF frequency 300 times the secular trapping frequency and the values of q are from 1×10^{-2} (lowest-infidelity trend) to 5×10^{-1} (highest-infidelity trend). The trap parameters are $\chi = 1.8 \times 10^{-4}$, $d = 100\ \mu$m, and $\frac{\omega}{2\pi} = 1$ MHz for both panels. Ideal gate infidelities without micromotion were roughly 10^{-12}, not shown on the scale of these plots. Increasing values of q indicate an increasing dynamic trapping potential $\tilde{U}$ and show a reduced fidelity. The dashed black line shows the fault-tolerant threshold of 2×10^{-4}. The dip in these plots corresponds to an optimum in minimizing the effects of micromotion. This optimum remains constant when the pulses occur at fixed points within the RF cycle, which is evidenced by the concurrence of these optima when the RF frequency is held constant with respect to the trapping frequency, as in (b).

favored for gate times that are multiples of half a trapping period [28]. The improvement is more significant for higher values of q, although it is not monotonic in the proximity of gate times that are multiples of half trap periods.

As stated at the end of Sec. III, not all choices of a and q depicted as stable in Fig. 4 will be stable in experiments. Stable trapping can be achieved with values of $q \sim 0.5$ which are used in current microtrap array implementations [36]. However, for these values to be useful for this scheme, a very careful selection of a and q is required in this region to appropriately align troughs in the RF oscillations to the

required pulse timings. This degree of control and freedom may be difficult to achieve in practice, which may limit the potential gate improvements. Even in these cases, it is still important to design the gates to account for the micromotion.

V. FINITE REPETITION RATE

The optimized gates shown in Fig. 6 assume perfect phase locking between the pulses and the RF drive, as well as large instantaneous momentum kicks. In practice, the pulse groups are composed of many small kicks. These small kicks can be
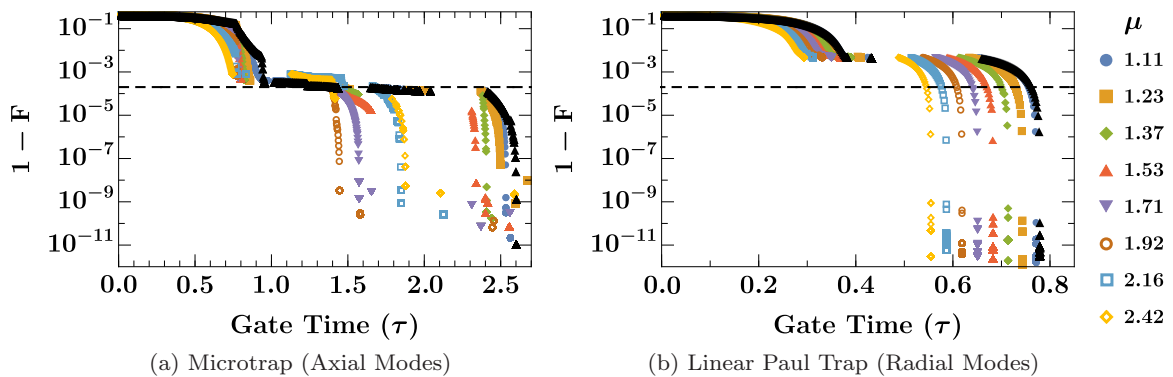

FIG. 6. Infidelities of optimized two-qubit gates with pulses occurring at the π phase to the RF drive, equivalent to a repetition rate locked to the trap RF drive frequency at this phase. Shown with increasing dynamic trapping potential $\tilde{U}$, indicated by increasing values of μ. (a) Microtrap architecture with $\chi = 1.8 \times 10^{-4}$ ($d = 100\ \mu$m, $\frac{\omega}{2\pi} = 1$ MHz) (b) Linear Paul trap using radial modes with $\chi = -1.4 \times 10^{-2}$ ($\omega_A / \omega_R = 1/6$). The results represented by black triangles indicate the infidelities for equivalent systems without the inclusion of micromotion. This shows that both systems benefit from a clear micromotion enhancement. The dashed black line shows the fault-tolerant threshold of 2×10^{-4}. The plateaus in the infidelity observed for some gate times can be attributed to the antisymmetric nature of the gate scheme, which is not favored for gate times that are multiples of half a trapping period. There is not a monotonic progression in (a) for some values of μ; this is due to the proximity of these results to half-multiples of the trapping period. These trends show that fast gates conducted with the aid of micromotion can be implemented with shorter gate times than gates conducted in the absence of micromotion.
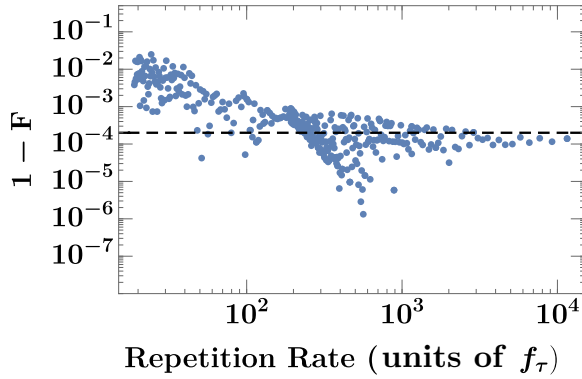
FIG. 7. The fidelity of an entangling gate that was designed with a repetition rate that is phase-locked to the RF drive, but implemented without this condition. The gate uses 50 counter-propagating pulse pairs ($n = 5$) and a total gate time of $\tau_G \sim 2$ trap periods. The dynamic trapping parameter for these data is $q = 0.2$, and the ratio between the RF driving frequency and the secular trapping frequency is $f_{RF}/f_\tau \approx 12$. This choice of parameters corresponds to a realistic trapping regime and shows that high-fidelity gate solutions can be found for current experimental traps.

made to occur near-simultaneously, using a series of optical delay loops [44]. However, this is experimentally complex and requires a high degree of accuracy in the pulse timings [28]. A simpler implementation method is to produce pulses at a fixed repetition rate and use a pulse picker to select a subset for use in the gates. We must examine the effects of this approximate implementation to ensure that it does not overly compromise the achievable fidelity of the gate.

Although our gate schemes are designed assuming that all the SDKs in the pulse groups occur instantaneously, in Fig. 7 we examine the effect of implementing them using nonsimultaneous pulses achievable with a finite repetition rate. In order to use physically reasonable choices of RF drive frequency, we adjust the pulse group timings of our gates to ensure our phase-locking condition. The resulting infidelity assuming an infinite repetition rate was $\sim 1 \times 10^{-4}$. This infidelity could be lowered by optimizing over the RF driving frequency. Implementing these gates with a finite repetition rate changes the fidelity significantly, but there are clearly a large number of high-fidelity solutions possible for realistic trapping parameters and for π-pulse repetition rates that have already been demonstrated [45].

Perhaps surprisingly, some of the gates implemented with a finite repetition rate, which are no longer technically phase locked, were actually better than the phase-locked gates. The large amount of scatter shows that these gate solutions are highly sensitive to variations in frequency, but even the upper edges of those solutions have promising fidelity.

VI. ROBUSTNESS

We now explore the robustness of these schemes to the inevitable imperfections in experimental implementations.

A. Finite temperature

We begin by first examining the impacts to gate fidelity as a result of higher-temperature ion crystals, in contrast to the
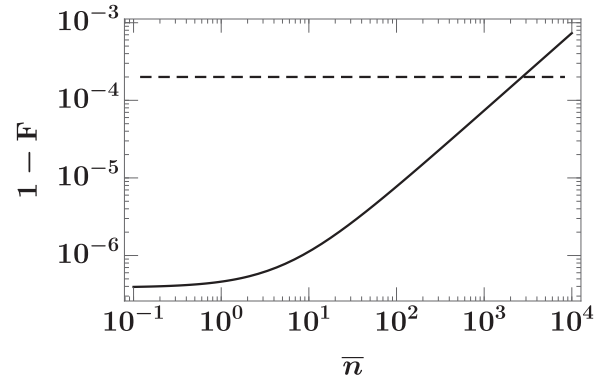

FIG. 8. Infidelity of FRAG gates under increasing mean motional occupation $\overline{n}$, assuming that the mean occupation is equal across all modes. This shows that these gates, and in fact any high-fidelity gate using ultrafast π pulses, remains robust to the temperature of the ion crystal. Certainly this will not be a limiting factor to gate fidelities in the Doppler cooling limit, where $\overline{n} \approx 10$.

ion crystals with a mean motional occupation of $\overline{n} = 0.1$ we have assumed until now. If we assume that each mode has the same mean motional occupation, the infidelity of an optimized gate can be expressed as a function of this mean occupation number. This is shown in Fig. 8, where it can be seen that the gate remains robust even with large motional occupation numbers of $\overline{n} = 100$. While this is shown for a FRAG gate, this is not unique to the FRAG scheme. This feature will be present in any scheme utilizing ultrafast counter-propagating π pulses.

In a similar vein, another form of error can arise due to motional heating during the gate operation. This form of error is investigated in more detail in [26]. This work showed that heating events during the gate operation would effectively destroy the gate operation, resulting in very low fidelities. This makes the motional heating an important experimental consideration, specifically, the motional heating on the modes that are coupled for a gate operation. As such, for gates operated on the radial modes, the motional heating in the axial modes will have little impact on the fidelity of these gates. And while the motional heating rate generally increases in longer ion chains, this does not necessarily result in an increase in the modes that are coupled during the gate operation.

B. Imperfect phase matching

We now examine what happens when the phase between the pulses arriving and the RF drive is not exactly π. As shown in Fig. 9(a), gates remain below error correction infidelity thresholds until there are phase mismatches of the order of $1/16$ of an RF period. The largest RF drives encountered in most experiments are of the order of 100 MHz, equating to a requirement for nanosecond accuracy of the pulse arrival time with respect to the maximum in the RF trapping potential.

C. Trap characterization

The next form of experimental error we examine is the effect of imprecise characterization of the trap, such as the trapping frequencies or distances between microtraps. Such
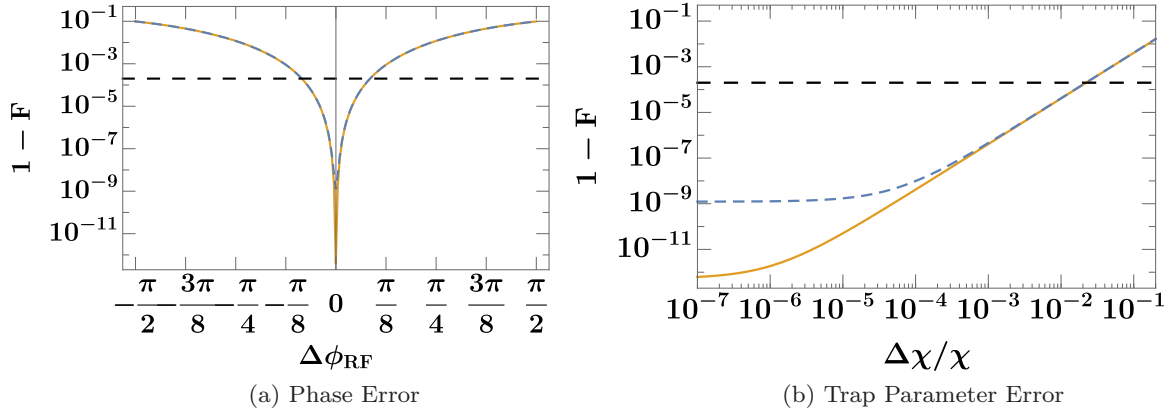
(a) Phase Error

(b) Trap Parameter Error

FIG. 9. Plots showing the impact on infidelity arising from realistic experimental errors for a gate with an ideal infidelity of 10^{-9} in a microtrap architecture, shown by the dashed blue line ($\chi = 1.3 \times 1.8 \times 10^{-4}$, $\tau_G = 1.0$, $n = 30$, $\mu = 2.31$), and a radial mode gate with an ideal infidelity of 10^{-13} on a linear Paul trap, shown by the orange line ($\chi = -1.3 \times 1.4 \times 10^{-2}$, $\tau_G = 0.7$, $n = 12$, $\mu = 2.31$). Here τ_G is the gate time and the multiplying factor of 1.3 is due to the effects of micromotion. (a) Errors in the phase between laser pulses and the RF drive. (b) Response to an error $\Delta\chi$ between the real value of χ and the value used to find an optimized gate. The dashed black line shows the fault-tolerant threshold of 2×10^{-4}.

errors would lead to an incorrect estimate of χ. Figure 9(b) shows that gates are also robust to such errors, remaining below error correction infidelity thresholds until errors of approximately 2% of the true value of χ, corresponding to an $\sim 0.5\%$ error in d or $\sim 1\%$ error in ω. In the case of the radial modes of a linear Paul trap, this corresponds to a 2% error in the ratio between the longitudinal and the radial trapping frequencies.

D. Imperfect pulses

Throughout the analysis of gate fidelities within this work we assume that each π pulse is perfect. In any experimental demonstration the π-pulse fidelity would be an important contributing factor to the overall fidelity. The worst-case impact of imperfect π pulses can be shown to result in a reduction in fidelity that scales linearly with the number of π pulses. This would give the overall fidelity F_{real} as

$$F_{\text{real}} \approx (1 - 2N_p\varepsilon)F_0, \tag{18}$$

where ε is the population transfer error for each π pulse, N_p is the total number of π-pulse pairs in the gate sequence, and F_0 is the gate fidelity assuming perfect π pulses. A detailed analysis of this error can be found here [46]. The gates presented in this paper required between 50 (Fig. 7) and 1000 π pulses. Therefore, to achieve the fault-tolerant threshold infidelity of 2×10^{-4}, a π-pulse error of between 2×10^{-6} and 2×10^{-8} would be necessary. The typical intensity stability of pulsed lasers is lower than this, but this only corresponds to pulse error when using square pulses. There are well-explored shaped pulses or multipulse schemes that correct the population transfer errors to first order [47,48]. Implementing them will be an extra experimental hurdle, but thereafter pulse errors should not limit the fast gates.

E. Stray fields

Finally, we consider the effects of stray fields on gate fidelities. Assuming that the stray fields vary slowly with respect to the RF drive frequency, this error will result in a

relative difference in the secular trapping frequencies between the two microtraps. This will be linearly proportional to the relative intensity of the stray field and the trapping fields. We simulate this error by applying a frequency offset to one of the trapping potentials and solving for the classical trajectories in phase space when the gate is applied. This is shown in Fig. 10, which shows that although the difference between the breathing mode and the common motional mode in a microtrap architecture is small ($\sim 10^{-4}$), correspondingly larger errors in the trapping frequencies ($\sim 10^{-3}$) of the individual traps do not result in significant fidelity loss. The relationship between a static stray field and the secular trapping frequency will be $\frac{\Delta\omega}{\omega} \sim \sqrt{2}\frac{\Delta E}{E}$. To conduct high-fidelity gates it is necessary to ensure that stray fields are no larger than 0.1%–0.2% of the applied voltages used to generate the trapping potential.

VII. CONCLUSION

We conclude that the micromotion present in ion trap experiments, either in microtraps or in linear Paul traps, may
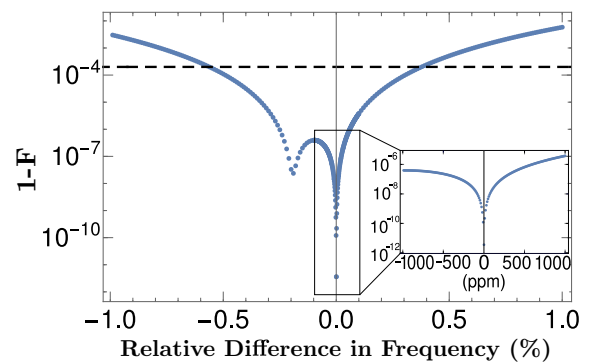

FIG. 10. The gate infidelity shown as a function of the difference in the secular trapping frequency between two harmonic trapping potentials, shown as the percentage difference in the main plot and the parts per million (ppm) difference in the inset.

be harnessed to enhance the gate times and infidelities of fast gates using ultrafast pulses. We have presented a technique to implement this enhancement by locking the RF drive and repetition rate and have also presented the conditions under which repetition rates faster than the RF drive may be used with a high fidelity. We have further shown that this method remains robust to realistic experimental errors that would be encountered when implementing such fast gates. Even in parameter regimes where the inclusion of micromotion makes only a small improvement, performing a high-fidelity fast gate requires it to be taken into account. Implementing the gates presented in this work requires considerable technical control over the ultrafast pulses, which will be made significantly easier as schemes are found with fewer required π-pulse pairs.

APPENDIX A: FIDELITY CALCULATIONS IN THE ABSENCE OF MICROMOTION

The material presented in this Appendix has been published in the Supplementary Material provided with [28] and is reproduced here with permission for ease of reading. We use numerical searches to find pulse timings that produce high-quality gate operations, with the state-averaged fidelity F, given as the integral of the square of the norm of the overlap between the postgate state and the target state integrated over all initial states. This is efficient to compute and it is strongly related to other distance measures for high-fidelity gates. As we examine fidelities extremely close to unity, we report the infidelity $1 - F$. This is a function of the phase mismatch $\Delta\phi$ around the target $\pi/4$ phase and the phase-space displacement of the motional modes ΔP_p given without micromotion as

$$\Delta P_p = 2\sqrt{\frac{\omega}{\omega_p}}\sum_k z_k \sin(\omega_p t_k),$$

$$\Delta\phi = \left|\sum_p 8\eta^2 \frac{\omega}{\omega_p} b_p^1 b_p^2 \sum_{i\neq j} z_i z_j \sin(\omega_p|t_i - t_j|)\right| - \frac{\pi}{4}.$$

(A1)

For efficient computation of two-ion gates, we further simplify this measure by using a truncated expansion of the infidelity in these variables. Assuming a thermal product state the infidelity is then given by

$$1 - F \approx \frac{2}{3}\Delta\phi^2 + \frac{4}{3}\sum_p \left(\frac{1}{2} + \bar{n}_p\right)\left((b_p^1)^2 + (b_p^2)^2\right)\Delta P_p^2,$$

(A2)

where $\bar{n}_p$ is the mean motional occupation of the pth mode. While this approximate form is efficient for generating gate

schemes, we use the full form when reporting achievable fidelities, for example, in the presence of multiple ions. We can see from Eq. (A3) that the infidelity for a two-ion system, $1 - F$, depends on the Lamb-Dicke parameter η, the angular frequencies' collective motional modes ω_n, the coupling of the kth ion to the pth mode, b_p^k, and the number of pulses in the ith pulse train z_i. The collective mode frequencies ω_n can be calculated from the mass of the ions M, the separation of the microtraps d, and the trapping frequency ω of the individual microtraps.

We search for pulse timings that produce the optimal gate fidelity within a given time bound. This optimization is run as a set of local gradient searches in the 3D parameter space of the pulse timings, over a large set of initial gate sequences. The highest fidelity of these local optimizations is then taken to be the optimal gate for that cap in the gate time. Note that the optimal gate occasionally takes less time than the maximum allowed. By increasing the cap on the total gate time and repeating this process, we map out the optimal fidelity for fast gates as a function of the gate time.

APPENDIX B: KEY PARAMETER FOR CHARACTERIZING TRAPS

The material presented in this Appendix has been previously published in the Supplementary Material provided with [28] and is reproduced here with permission for ease of reading. We see from Eq. (A3) that the system behavior depends on the ratios of the frequencies of the collective modes. These are in turn functions of the geometry, and the dimensionless parameter $\xi = \frac{d^3\omega^2}{\alpha}$, where $\alpha = \frac{e^2}{4\pi\varepsilon_0}\frac{1}{M}$. Here e is the electron charge, M the mass of the ions, and ε_0 the vacuum permittivity.

For a two-ion system, there is only one ratio, so it entirely characterizes the behavior. We define χ as the normalized difference between the breathing mode frequency and the common motional mode frequency $\chi = \frac{\omega_{BR} - \omega}{\omega}$, which can be expressed in terms of the more fundamental parameter ξ as

$$\chi = \sqrt{\frac{1}{3}\left(9 - \beta\gamma^{\frac{1}{3}} + \beta\gamma^{\frac{2}{3}}\right)} - 1,$$

(B1)

where

$$\gamma = 1 + \frac{3(9 + \sqrt{3}\sqrt{27 + 2\xi})}{\xi}$$

and

$$\beta = 9 - \sqrt{3}\sqrt{27 + 2\xi}.$$

Its value lies in the range between 0 and $\sqrt{3} - 1$. The upper bound corresponds to the limit where both microtraps are merged, which is the case for standard linear trap geometries.

When gates are conducted using the radial modes of ions cotrapped in a linear Paul trap, the relevant ratio is that between the rocking mode frequency ω_R and the common motional mode frequency in the transverse axis ω_T. Taking the ratio of the axial and radial trapping frequencies to be $\kappa = \omega_A/\omega_T$, the rocking mode frequency will then be

$\omega_R = (1 - \kappa)\omega_T$. The parameter χ will then be given by

$$\chi = \sqrt{1 - \kappa^2} - 1. \tag{B2}$$

In this case the value of χ will be between -1 and 0. The negative value of χ indicates a negative rate of phase acquisition compared to the microtrap system or the longitudinal modes of a linear Paul trap.

Even for three or more ions, the system is still well characterized by χ, which is the normalized gap to the lowest energy excitation in the system. This is because it defines the rate of relative acquisition of phase between the excited and the unexcited modes.

APPENDIX C: FIDELITY CALCULATIONS IN THE PRESENCE OF MICROMOTION

To determine the correct expression for the fidelity we start by deriving the positions and velocities of the ions under a set of initial conditions. We do this for a general set of modes, defined by frequencies ω, which makes this derivation suitable for both microtraps and radial kicks for ions in a common linear Paul trap. We then use this to derive an expression for the phase acquired at the end of a series of instantaneous momentum kicks. The displacement from equilibrium of a single ion with initial position and velocity x_0 and v_0, respectively, at time $\tau = 0$ in dimensionless time will be given by

$$x_{i,p}(\tau) = \frac{2\beta}{\rho} v_0 \frac{\omega}{\omega_p} \left(\sin\left(2\pi \frac{\omega_p}{\omega}\tau\right)(\sigma_c f_c(\tau) + \sigma_s f_s(\tau)) + \cos\left(2\pi \frac{\omega_p}{\omega}\tau\right)(\sigma_c f_s(\tau) - \sigma_s f_c(\tau)) \right)$$

$$+ \frac{2\beta}{\rho} 4\pi x_0 \frac{\omega}{\omega_p} \sin\left(2\pi \frac{\omega_p}{\omega}\tau\right)(\beta\sigma_s f_c(\tau) + 2f_c(\tau)\zeta_s - \beta\sigma_c f_s(\tau) - 2f_s(\tau)\zeta_c)$$

$$+ \frac{2\beta}{\rho} 4\pi x_0 \frac{\omega}{\omega_p} \cos\left(2\pi \frac{\omega_p}{\omega}\tau\right)(\beta\sigma_c f_c(\tau) + 2f_c(\tau)\zeta_c + \beta\sigma_s f_s(\tau) + 2f_s(\tau)\zeta_s), \tag{C1}$$

where x_0 and v_0 have the same units, as dimensionless time is being used,

$$f_c(\tau) = \sum_{j=-\infty}^{\infty} C_j \cos\left(\frac{4j\pi\tau}{\beta} + j\phi_{\text{RF}}\right),$$

$$f_s(\tau) = \sum_{j=-\infty}^{\infty} C_j \sin\left(\frac{4j\pi\tau}{\beta} + j\phi_{\text{RF}}\right),$$

$$\sigma_c = \sum_{j=-\infty}^{\infty} C_j \cos(j\phi_{\text{RF}}),$$

$$\sigma_s = \sum_{j=-\infty}^{\infty} C_j \sin(j\phi_{\text{RF}}),$$

$$\zeta_c = \sum_{j=-\infty}^{\infty} jC_j \cos(j\phi_{\text{RF}}),$$

$$\zeta_s = \sum_{j=-\infty}^{\infty} jC_j \sin(j\phi_{\text{RF}}),$$

$$\rho = 4\pi(\sigma_c(\beta\sigma_c + 2\zeta_c) + \sigma_s(\beta\sigma_s + 2\zeta_s)), \tag{C2}$$

and the coefficients C_j are given through the recurrence relationship shown below, obtained by substituting the solution into the ODE governing the motion:

$$C_{j+1} - D_j C_j + C_{j-1} = 0,$$
$$D_j = (a_x - (2j + \beta)^2)/q_x. \tag{C3}$$

By applying all pulses at the same fixed phase ϕ_{RF} in the micromotion cycle, the micromotion terms can be taken as a constant factor in the expression with $f_c(\tau) = \sigma_c$ and $f_s(\tau) = \sigma_s$. When we then consider the effect of an instantaneous pulse group imparting momentum v_0 at time $\tau = 0$ the expression for the following motion will be given by

$$x_{i,p}(\tau) = \frac{2\beta}{\rho} \left(v_0(\sigma_c^2 + \sigma_s^2) + 4\pi x_0(2\sigma_c\zeta_s - 2\sigma_s\zeta_c)\right) \sin\left(2\pi \frac{\omega_p}{\omega}\tau\right) + 8\beta\pi x_0 \cos\left(2\pi \frac{\omega_p}{\omega}\tau\right), \tag{C4}$$

and the velocity by

$$v_{i,p}(\tau) = \frac{4\pi}{\rho} v_0 \cos(2\pi\tau)(\sigma_c(\beta\sigma_c + 2\zeta_c) + \sigma_s(\beta\sigma_s + 2\zeta_s)) + \frac{4\pi}{\rho} v_0 \sin(2\pi\tau)(\sigma_s\zeta_c - \sigma_c\zeta_s)$$

$$- \frac{4\pi}{\rho} 2\pi\beta x_0 \frac{\omega}{\omega_p} \sin(2\pi\tau)\left(4\beta\sigma_c\zeta_c + 4\beta\sigma_s\zeta_s + 4(\zeta_s^2 + \zeta_c^2) + \beta^2\sigma_c^2 + \beta^2\sigma_s^2\right). \tag{C5}$$

After a series of instantaneous momentum kicks $\{P_j\}$ at times $\{\tau_j\}$ the position after the mth kick will be given by

$$x_{i,p,m}(\tau) = \frac{2\beta(\sigma_c^2 + \sigma_s^2)}{\rho} \frac{\omega}{\omega_p} \sum_{j=1}^{m} P_j \sin\left(2\pi \frac{\omega_p}{\omega}(\tau - \tau_j)\right) \tag{C6}$$

and the velocity will be given by

$$v_{i,p,m}(\tau) = \frac{4\pi}{\rho}\left(2\sigma_c\zeta_c + 2\sigma_s\zeta_s + \beta\sigma_c^2 + \beta\sigma_s^2\right)\sum_{j=1}^{m} P_j \cos\left(2\pi \frac{\omega_p}{\omega}(\tau - \tau_j)\right) + \frac{4\pi}{\rho}(\sigma_s\zeta_c - \sigma_c\zeta_s)\sum_{j=1}^{m} P_j \sin\left(2\pi \frac{\omega_p}{\omega}(\tau - \tau_j)\right)$$

$$= \sum_{j=1}^{m} P_j \cos\left(2\pi \frac{\omega_p}{\omega}(\tau - \tau_j)\right) + \frac{4\pi}{\rho}(\sigma_s\zeta_c - \sigma_c\zeta_s)\sum_{j=1}^{m} P_j \sin\left(2\pi \frac{\omega_p}{\omega}(\tau - \tau_j)\right). \tag{C7}$$

The geometric phase from a sequence of n pulses will be given by

$$\xi = \sum_{k}^{n-1}\sum_{i,p}(x_{i,p,k}(\tau_{k+1})v_{i,p,k}(\tau_{k+1}) - x_{i,p,k}(\tau_k)v_{i,p,k}(\tau_k))$$

$$= \frac{2\beta(\sigma_c^2 + \sigma_s^2)}{\rho}\sum_{k}^{n-1}\sum_{i,p}\left(\frac{\omega}{\omega_p}\sum_{j=1}^{k} P_j \sin\left(2\pi \frac{\omega_p}{\omega}(\tau_{k+1} - \tau_j)\right)\sum_{j=1}^{k} P_j \cos\left(2\pi \frac{\omega_p}{\omega}(\tau_{k+1} - \tau_j)\right)\right.$$

$$\left. - \frac{\omega}{\omega_p}\sum_{j=1}^{k} P_j \sin\left(2\pi \frac{\omega_p}{\omega}(\tau_k - \tau_j)\right)\sum_{j=1}^{k} P_j \cos\left(2\pi \frac{\omega_p}{\omega}(\tau_k - \tau_j)\right)\right.$$

$$\left. + \frac{4\pi}{\rho}(\sigma_s\zeta_c - \sigma_c\zeta_s)\frac{\omega}{\omega_p}\left(\left(\sum_{j=1}^{m} P_j \sin\left(2\pi \frac{\omega_p}{\omega}(\tau_{k+1} - \tau_j)\right)\right)^2 - \left(\sum_{j=1}^{m} P_j \sin\left(2\pi \frac{\omega_p}{\omega}(\tau_k - \tau_j)\right)\right)^2\right)\right). \tag{C8}$$

The double sine terms can then be shown to be equivalent to the motional restoration term. This term will be small, as part of our optimization objective is to obtain motional restoration and, thus, can be neglected. Giving the expression for ξ as

$$\xi = \frac{2\beta(\sigma_c^2 + \sigma_s^2)}{\rho}\sum_{k}^{n-1}\sum_{i,p}\left(\frac{\omega}{\omega_p}\sum_{j=1}^{k} P_j \sin\left(2\pi \frac{\omega_p}{\omega}(\tau_{k+1} - \tau_j)\right)\sum_{j=1}^{k} P_j \cos\left(2\pi \frac{\omega_p}{\omega}(\tau_{k+1} - \tau_j)\right)\right.$$

$$\left. + \frac{\omega}{\omega_p}\sum_{j=1}^{k} P_j \sin\left(2\pi \frac{\omega_p}{\omega}(\tau_k - \tau_j)\right)\sum_{j=1}^{k} P_j \cos\left(2\pi \frac{\omega_p}{\omega}(\tau_k - \tau_j)\right)\right). \tag{C9}$$

We denote the phase expression for an equivalent system without micromotion as ξ_0, given as

$$\xi_0 = \sum_{k}^{n-1}\sum_{i,p}\left(\frac{\omega}{\omega_p}\sum_{j=1}^{k} P_j \sin\left(2\pi \frac{\omega_p}{\omega}(\tau_{k+1} - \tau_j)\right)\sum_{j=1}^{k} P_j \cos\left(2\pi \frac{\omega_p}{\omega}(\tau_{k+1} - \tau_j)\right)\right.$$

$$\left. + \frac{\omega}{\omega_p}\sum_{j=1}^{k} P_j \sin\left(2\pi \frac{\omega_p}{\omega}(\tau_k - \tau_j)\right)\sum_{j=1}^{k} P_j \cos\left(2\pi \frac{\omega_p}{\omega}(\tau_k - \tau_j)\right)\right); \tag{C10}$$

the phase with micromotion can now be expressed as

$$\xi = \frac{\beta(\sigma_c^2 + \sigma_s^2)}{(\sigma_c(\beta\sigma_c + 2\zeta_c) + \sigma_s(\beta\sigma_s + 2\zeta_s))}\xi_0. \tag{C11}$$

We can then define the term μ giving the increase in the maximum displacement D' of the ion within the micromotion system after an instantaneous pulse, scaled to the maximum displacement of the same system without micromotion D,

$$\mu = \frac{D' - D}{D} = \frac{\beta(\sigma_c^2 + \sigma_s^2)}{(\sigma_c(\beta\sigma_c + 2\zeta_c) + \sigma_s(\beta\sigma_s + 2\zeta_s))}, \tag{C12}$$

giving the phase expression as

$$\xi = \mu\xi_0. \tag{C13}$$

The infidelity expression $1 - F$, the motional restoration of the pth mode ΔP_p, and the phase error $\Delta \phi$ will be given as

$$1 - F \approx \frac{2}{3} \Delta \phi^2 + \frac{4}{3} \sum_p \left(\frac{1}{2} + \overline{n}_p \right) \left((b_p^1)^2 + (b_p^2)^2 \right) \Delta P_p^2,$$

$$\Delta P_p = 2\mu \sqrt{\frac{\omega}{\omega_p}} \sum_k z_k \sin(\omega_p t_k),$$

$$\Delta \phi = \left| \sum_p 8\eta^2 \mu \frac{\omega}{\omega_p} b_p^1 b_p^2 \sum_{i \neq j} z_i z_j \sin(\omega_p |t_i - t_j|) \right| - \frac{\pi}{4}. \tag{C14}$$

[1] M. A. Nielsen and I. L. Chuang, *Quantum Computation and Quantum Information* (Cambridge University Press, Cambridge, UK, 2010), p. 702.

[2] Y. Makhlin, G. Scöhn, and A. Shnirman, Josephson-junction qubits with controlled couplings, Nature **398**, 305 (1999).

[3] P. Neumann, N. Mizuochi, F. Rempp, P. Hemmer, H. Watanabe, S. Yamasaki, V. Jacques, T. Gaebel, F. Jelezko, and J. Wrachtrup, Multipartite entanglement among single spins in diamond, Science **320**, 1326 (2008).

[4] E. Knill, R. Laflamme, and G. J. Milburn, A scheme for efficient quantum computation with linear optics, Nature **409**, 46 (2001).

[5] D. G. Cory, A. F. Fahmy, and T. F. Havel, Ensemble quantum computing by NMR spectroscopy, Proc. Natl. Acad. Sci. USA **94**, 1634 (1997).

[6] C. Nayak, S. H. Simon, A. Stern, M. Freedman, and S. Das Sarma, Non-Abelian anyons and topological quantum computation, Rev. Mod. Phys. **80**, 1083 (2008).

[7] D. Loss and D. P. DiVincenzo, Quantum computation with quantum dots, Phys. Rev. A **57**, 120 (1998).

[8] B. E. Kane, A silicon-based nuclear spin quantum computer, Nature **393**, 133 (1998).

[9] A. G. Fowler, M. Mariantoni, J. M. Martinis, and A. N. Cleland, Surface codes: Towards practical large-scale quantum computation, Phys. Rev. A **86**, 032324 (2012).

[10] D. P. DiVincenzo, The physical implementation of quantum computation, Fortschr. Phys. **48**, 771 (2000).

[11] G. Waldherr, Y. Wang, S. Zaiser, M. Jamali, T. Schulte-Herbrüggen, H. Abe, T. Ohshima, J. Isoya, J. F. Du, P. Neumann, and J. Wrachtrup, Quantum error correction in a solid-state hybrid spin register, Nature **506**, 204 (2014).

[12] M. Veldhorst, J. C. C. Hwang, C. H. Yang, A. W. Leenstra, B. de Ronde, J. P. Dehollain, J. T. Muhonen, F. E. Hudson, K. M. Itoh, A. Morello, and A. S. Dzurak, An addressable quantum dot qubit with fault-tolerant control-fidelity, Nat. Nanotechnol. **9**, 981 (2014).

[13] F. Dolde, V. Bergholm, Y. Wang, I. Jakobi, B. Naydenov, S. Pezzagna, J. Meijer, F. Jelezko, P. Neumann, T. Schulte-Herbrüggen, J. Biamonte, and J. Wrachtrup, High-fidelity spin entanglement using optimal control, Nat. Commun. **5**, 3371 (2014).

[14] R. Barends, J. Kelly, A. Megrant, A. Veitia, D. Sank, E. Jeffrey, T. C. White, J. Mutus, A. G. Fowler, B. Campbell, Y. Chen, Z. Chen, B. Chiaro, A. Dunsworth, C. Neill, P. O'Malley, P. Roushan, A. Vainsencher, J. Wenner, A. N. Korotkov, A. N. Cleland, and J. M. Martinis, Superconducting quantum circuits at the surface code threshold for fault tolerance, Nature **508**, 500 (2014).

[15] N. Friis, O. Marty, C. Maier, C. Hempel, M. Holzäpfel, P. Jurcevic, M. B. Plenio, M. Huber, C. Roos, R. Blatt, and B. Lanyon, Observation of Entangled States of a Fully Controlled 20-Qubit System, Phys. Rev. X **8**, 021012 (2018).

[16] C. Hempel, C. Maier, J. Romero, J. McClean, T. Monz, H. Shen, P. Jurcevic, B. P. Lanyon, P. Love, R. Babbush, A. Aspuru-Guzik, R. Blatt, and C. F. Roos, Quantum Chemistry Calculations on a Trapped-Ion Quantum Simulator, Phys. Rev. X **8**, 031022 (2018).

[17] D. Nigg, M. Muller, E. A. Martinez, P. Schindler, M. Hennrich, T. Monz, M. A. Martin-Delgado, and R. Blatt, Quantum computations on a topologically encoded qubit, Science **345**, 302 (2014).

[18] J. Zhang, G. Pagano, P. W. Hess, A. Kyprianidis, P. Becker, H. Kaplan, A. V. Gorshkov, Z.-X. Gong, and C. Monroe, Observation of a many-body dynamical phase transition with a 53-qubit quantum simulator, Nature **551**, 601 (2017).

[19] P. Brooks and J. Preskill, Fault-tolerant quantum computation with asymmetric Bacon-Shor codes, Phys. Rev. A **87**, 032310 (2013).

[20] C. J. Ballance, T. P. Harty, N. M. Linke, M. A. Sepiol, and D. M. Lucas, High-Fidelity Quantum Logic Gates Using Trapped-Ion Hyperfine Qubits, Phys. Rev. Lett. **117**, 060504 (2016).

[21] J. P. Gaebler, T. R. Tan, Y. Lin, Y. Wan, R. Bowler, A. C. Keith, S. Glancy, K. Coakley, E. Knill, D. Leibfried, and D. J. Wineland, High-Fidelity Universal Gate Set for ^{9}Be$^+$ Ion Qubits, Phys. Rev. Lett. **117**, 060505 (2016).

[22] C. H. Baldwin, B. J. Bjork, J. P. Gaebler, D. Hayes, and D. Stack, Subspace benchmarking high-fidelity entangling operations with trapped ions, Phys. Rev. Research **2**, 013317 (2020).

[23] J. Casanova, A. Mezzacapo, L. Lamata, and E. Solano, Quantum Simulation of Interacting Fermion Lattice Models in Trapped Ions, Phys. Rev. Lett. **108**, 190502 (2012).

[24] J. J. García-Ripoll, P. Zoller, and J. I. Cirac, Coherent control of trapped ions using off-resonant lasers, Phys. Rev. A **71**, 062309 (2005).

[25] L.-M. Duan, Scaling Ion Trap Quantum Computation Through Fast Quantum Gates, Phys. Rev. Lett. **93**, 100502 (2004).

[26] R. L. Taylor, C. D. B. Bentley, J. S. Pedernales, L. Lamata, E. Solano, A. R. R. Carvalho, and J. J. Hope, A study on fast gates for large-scale quantum simulation with trapped ions, Sci. Rep. **7**, 46197 (2017).

[27] C. D. B. Bentley, A. R. R. Carvalho, and J. J. Hope, Trapped ion scaling with pulsed fast gates, New J. Phys. **17**, 103025 (2015).

[28] A. K. Ratcliffe, R. L. Taylor, J. J. Hope, and A. R. R. Carvalho, Scaling Trapped Ion Quantum Computers Using Fast Gates and Microtraps, Phys. Rev. Lett. **120**, 220501 (2018).

[29] K. G. Johnson, J. D. Wong-Campos, B. Neyenhuis, J. Mizrahi, and C. Monroe, Ultrafast creation of large Schrödinger cat states of an atom, Nat. Commun. **8**, 697 (2017).

[30] J. D. Wong-Campos, S. A. Moses, K. G. Johnson, and C. Monroe, Demonstration of Two-Atom Entanglement with Ultrafast Optical Pulses, Phys. Rev. Lett. **119**, 230501 (2017).

[31] V. M. Schäfer, C. J. Ballance, K. Thirumalai, L. J. Stephenson, T. G. Ballance, A. M. Steane, and D. M. Lucas, Fast quantum logic gates with trapped-ion qubits, Nature **555**, 75 (2018).

[32] E. Shimshoni, G. Morigi, and S. Fishman, Quantum Zigzag Transition in Ion Chains, Phys. Rev. Lett. **106**, 010401 (2011).

[33] D. Leibfried, R. Blatt, C. Monroe, and D. Wineland, Quantum dynamics of single trapped ions, Rev. Mod. Phys. **75**, 281 (2003).

[34] C. Shen and L.-M. Duan, High-fidelity quantum gates for trapped ions under micromotion, Phys. Rev. A **90**, 022332 (2014).

[35] A. Bermudez, P. Schindler, T. Monz, R. Blatt, and M. Müller, Micromotion-enabled improvement of quantum logic gates with trapped ions, New J. Phys. **19**, 113038 (2017).

[36] M. Kumph, P. Holz, K. Langer, M. Meraner, M. Niedermayr, M. Brownnutt, and R. Blatt, Operation of a planar-electrode ion-trap array with adjustable RF electrodes, New J. Phys. **18**, 023047 (2016).

[37] H. Landa, M. Drewsen, B. Reznik, and A. Retzker, Modes of oscillation in radiofrequency Paul traps, New J. Phys. **14**, 093023 (2012).

[38] J. J. Garcia-Ripoll, P. Zoller, and J. I. Cirac, Fast and Robust Two-Qubit Gates for Scalable Ion Trap Quantum Computing, Phys. Rev. Lett. **91**, 157901 (2003).

[39] C. D. B. Bentley, R. L. Taylor, A. R. R. Carvalho, and J. J. Hope, Stability thresholds and calculation techniques for fast entangling gates on trapped ions, Phys. Rev. A **93**, 042342 (2016).

[40] I. V. Inlek, C. Crocker, M. Lichtman, K. Sosnova, and C. Monroe, Multispecies Trapped-Ion Node for Quantum Networking, Phys. Rev. Lett. **118**, 250502 (2017).

[41] A. Drakoudis, M. Söllner, and G. Werth, Instabilities of ion motion in a linear Paul trap, Int. J. Mass Spectrom. **252**, 61 (2006).

[42] R. Alheit, T. Gudjons, S. Kleineidam, and G. Werth, Some observations on higher-order non-linear resonances in a Paul trap, Rapid Commun. Mass Spectrom. **10**, 583 (1996).

[43] B. A. Collings and D. J. Douglas, Observation of higher order quadrupole excitation frequencies in a linear ion trap, J. Am. Soc. Mass Spectrom. **11**, 1016 (2000).

[44] C. D. B. Bentley, A. R. R. Carvalho, D. Kielpinski, and J. J. Hope, Fast gates for ion traps by splitting laser pulses, New J. Phys. **15**, 043006 (2013).

[45] D. Heinrich, M. Guggemos, M. Guevara-Bertsch, M. I. Hussain, C. F. Roos, and R. Blatt, Ultrafast coherent excitation of a ^{40}Ca$^+$ ion, New J. Phys. **21**, 073017 (2019).

[46] E. P. G. Gale, Z. Mehdi, L. M. Oberg, A. K. Ratcliffe, S. A. Haine, and J. J. Hope, Optimised fast gates for quantum computing with trapped ions, arXiv:1912.07780.

[47] C. Kabytayev, T. J. Green, K. Khodjasteh, M. J. Biercuk, L. Viola, and K. R. Brown, Robustness of composite pulses to time-dependent control noise, Phys. Rev. A **90**, 012316 (2014).

[48] L. M. K. Vandersypen and I. L. Chuang, NMR techniques for quantum control and computation, Rev. Mod. Phys. **76**, 1037 (2005).